MISTRAL: a myopic edge-preserving image restoration method, with application to astronomical adaptive-optics-corrected long-exposure images

Laurent M. Mugnier, Thierry Fusco, and Jean-Marc Conan

Office National d'Études et de Recherches Aérospatiales, Optics Department, B.P. 72, F-92322 Châtillon cedex, France

Received August 8, 2003; revised manuscript received April 14, 2004; accepted April 15, 2004

Deconvolution is a necessary tool for the exploitation of a number of imaging instruments. We describe a deconvolution method developed in a Bayesian framework in the context of imaging through turbulence with adaptive optics. This method uses a noise model that accounts for both photonic and detector noises. It additionally contains a regularization term that is appropriate for objects that are a mix of sharp edges and smooth areas. Finally, it reckons with an imperfect knowledge of the point-spread function (PSF) by estimating the PSF jointly with the object under soft constraints rather than blindly (i.e., without constraints). These constraints are designed to embody our knowledge of the PSF. The implementation of this method is called MISTRAL. It is validated by simulations, and its effectiveness is illustrated by deconvolution results on experimental data taken on various adaptive optics systems and telescopes. Some of these deconvolutions have already been used to derive published astrophysical interpretations.

OCIS codes: 100.1830, 100.3020, 100.3190, 010.1080, 010.1330, 110.6770.

1. INTRODUCTION

The performance of high-resolution imaging with large astronomical telescopes is severely limited by atmospheric turbulence. Adaptive optics[1–3] (AO) offers real-time compensation of the turbulence. The correction is, however, only partial,[2,4–7] and the long-exposure images must be deconvolved to restore the fine details of the object.

Because of the inevitable noise in the images, great care must be taken in the deconvolution process to obtain a reliable restoration with good photometric precision. A key point is to recognize that noise makes it necessary to add some prior knowledge on the observed object into the deconvolution method; failure to do so usually results in unacceptable amplification of the noise.[8,9] Additionally, fine modeling of the noise statistics contributes to the accurate restoration of objects with a high dynamic range. Finally, the fact that the residual point-spread function (PSF) is usually not perfectly known[10,11] adds to the difficulty.

This paper presents a deconvolution method that falls within the maximum *a posteriori* (MAP) framework, or, equivalently, the penalized-likelihood framework, and that addresses these three points. It uses a prior that is well adapted to astronomical objects that are a mix of sharp structures and smooth areas, such as planets and asteroids; for pointlike objects such as binary stars, an alternative and more appropriate prior can be used. This method takes into account the presence of a mixture of photon and electronic noises. It also estimates the PSF given some prior information on the average PSF and its variability. The implementation of this method is called MISTRAL (for Myopic Iterative STep-preserving Restoration ALgorithm). Although it is presented in the context of long-exposure images recorded on AO-corrected telescopes, this method can be used in other contexts as well. In particular, it has already been successfully used for Hubble Space Telescope data.[12]

2. IMAGING MODEL AND PROBLEM STATEMENT

Within the isoplanatic angle, defined as the size of the angular patch in which the PSF due to turbulence can be considered constant, the image i of the observed object o at the focal plane of the system consisting of the atmosphere, the telescope, the AO system and the detector is given by

$$i = [h * o] \diamond n, \tag{1}$$

where $*$ denotes the convolution operator and $[\cdot]$ the sampling operator, h is the PSF of the system, n is a corruptive noise process (often predominantly photon noise), and the symbol $\diamond$ represents a pixel-by-pixel operation.[8] If the noise is additive and independent of the noiseless image $[h * o]$, then the symbol $\diamond$ simply represents addition.

In the following sections we shall consider that the object and the image are sampled on a regular grid, yielding a vectorial formulation for Eq. (1):

$$\mathbf{i} = (\mathbf{h} * \mathbf{o}) \diamond \mathbf{n}, \tag{2}$$

where $\mathbf{o}$, $\mathbf{i}$, and $\mathbf{n}$ are the vectors corresponding to the lexicographically ordered object, image, and noise, respectively.

1084-7529/2004/101841-14$15.00

Note that the raw image must be carefully preprocessed to yield an image that closely follows this imaging model. The preprocessing includes at least the correction of the background and of the flat field, the correction of the camera's bad pixels and possibly of its correlated noise, and the scaling of the image in photons. In the case of background-dominated (e.g., thermal infrared) images, one must often record tens of images to avoid detector saturation. The preprocessing then includes the (relative) recentering of these images[13] and their addition prior to deconvolution. One could contemplate processing these images jointly rather than co-adding them. Yet for AO-corrected images this would be costly in computation time while bringing very little additional information, because all PSFs are essentially the same as soon as the exposure time is long with respect to the evolution time scale of turbulence.

The deconvolution procedure needs a measurement of the PSF. The usual procedure consists in recording the corrected image of a nearby unresolved star shortly before and/or after observing the object of interest. Since the correction quality depends on the observing conditions (turbulence strength, wind speed, magnitude, and spatial extent of the source used for wave-front sensing), the unresolved star image is not a perfect measurement of the PSF associated with the image to be deconvolved.[10] A more precise estimate of the PSF can be obtained via control-loop data accumulated during the acquisition of the object of interest.[14] The PSF estimated in this fashion still has a limited precision owing to noise and corresponds to an infinite integration time, so it is also imperfect. Furthermore, it does not intrinsically include the effect of static aberrations, even though these can be calibrated either by using the image of a star and its control-loop data[14] or by a dedicated setup of the instrument.[15,16]

The problem is to obtain an estimate $\hat{\mathbf{o}}$ of the observed object $\mathbf{o}$ given the image $\mathbf{i}$, a more-or-less precise knowledge of the PSF $\mathbf{h}$, and some prior information on the noise statistics and on the object.

3. DECONVOLUTION APPROACH

A. Deconvolution with Known Point-Spread Function

We first address the classical case in which the PSF is assumed to be known. Most deconvolution techniques boil down to the minimization (or maximization) of a criterion. The first issue is the definition of a suitable criterion for the given inverse problem. The second issue is then to find the position of the criterion's global minimum, which is defined as the solution. This second issue will be addressed in Section 4.

Following the probabilistic (Bayesian) MAP approach, the deconvolution problem can be stated as follows: We look for the most likely object $\hat{\mathbf{o}}$ given the observed image $\mathbf{i}$ and our prior information on $\mathbf{o}$, which is summarized by a probability density $p(\mathbf{o})$. This reads as

$$\hat{\mathbf{o}} = \arg\max_{\mathbf{o}} p(\mathbf{o}|\mathbf{i}) = \arg\max_{\mathbf{o}} p(\mathbf{i}|\mathbf{o}) \times p(\mathbf{o}). \quad (3)$$

Equivalently, $\hat{\mathbf{o}}$ can be defined as the object that minimizes a compound criterion $J(\mathbf{o})$ defined as follows:

$$J(\mathbf{o}) = J_i(\mathbf{o}) + J_o(\mathbf{o}), \quad (4)$$

where the negative log-likelihood $J_i = -\ln p(\mathbf{i}|\mathbf{o})$ is a measure of fidelity to the data and $J_o = -\ln p(\mathbf{o})$ is a regularization or penalty term, so the MAP solution can equivalently be called a penalized-likelihood solution. Note that the Bayesian approach does not require that $\mathbf{o}$ truly be the outcome of a stochastic process; rather, $p(\mathbf{o})$ should be designed to embody the available prior information on $\mathbf{o}$, which means that J_o should have higher values for objects that are less compatible with our prior knowledge,[8] e.g., that are very oscillating. When $\mathbf{o}$ is not the outcome of a stochastic process, J_o usually includes a scaling factor or global hyperparameter, denoted by μ in the following, which adjusts the balance between fidelity to the data and fidelity to the prior information.

If no prior knowledge is used, which corresponds to setting $p(\mathbf{o})$ = constant in Eq. (3), one then maximizes $p(\mathbf{i}|\mathbf{o})$ (likelihood of the data) so that the solution is a maximum-likelihood solution. In this case the criterion of Eq. (4) is constituted only of the term J_i. The Richardson–Lucy algorithm[17] is an example of an iterative algorithm that converges toward the minimum of J_i when the noise follows Poisson statistics.

1. Noise Model

If the noise statistics are additive, stationary, white Gaussian, then the data fidelity term is J_i^{swG}, a simple least-squares difference between the actual data $\mathbf{i}$ and our model of the data for a given object, $\mathbf{h}*\mathbf{o}$.

In astronomical imaging, the noise is often predominantly photon noise, which follows Poisson statistics and has the following negative log-likelihood:

$$J_i^P(\mathbf{o}) = \sum_{l,m} (\mathbf{h}*\mathbf{o})(l, m) - \mathbf{i}(l, m)\ln[(\mathbf{h}*\mathbf{o})(l, m)], \quad (5)$$

where the sum extends over all pixels (l, m) of the image. This model can perform notably better than simple least-squares for objects with high dynamic range on a dark background, because the noise variance $(\mathbf{h}*\mathbf{o})(l, m)$ varies strongly between pixels for images of such objects. Yet in dark regions of the image the noise is usually predominantly detector noise, which follows Gaussian, and approximately stationary, statistics. A fine noise model should thus take into account both components of the noise.[18]

This is why we adopt a nonstationary white Gaussian model for the noise, which is a good approximation of a mix of photon and detector noise:

$$J_i^{\mathrm{mix}}(\mathbf{o}) = \sum_{l,m} \frac{1}{2\sigma^2(l, m)}[\mathbf{i}(l, m) - (\mathbf{o}*\mathbf{h})(l, m)]^2, \quad (6)$$

where $\sigma^2(l, m) = \sigma_{\mathrm{ph}}^2 + \sigma_{\mathrm{det}}^2$ is the sum of the photon noise and the detector noise variance. In the absence of detector noise, J_i^{mix} from Eq. (6) is actually a second-order expansion of J_i^P defined in Eq. (5). Additionally, from our experience, the use of J_i^{mix} rather than J_i^P makes the com-

putation of the solution with gradient-based techniques faster. We believe that this can be attributed to the fact that J_i^{mix} is quadratic.

The variance σ_{det}^2 and the variance map $\sigma_{\text{ph}}^2(l, m)$ can both be estimated from the image. Currently we estimate σ_{det}^2 by fitting the histogram of negative-valued pixels with the left half of a centered Gaussian, which leads to

$$\sigma_{\text{det}}^2 = \frac{\pi}{2}[\langle \mathbf{i}(l, m)\rangle_{((l,m);\mathbf{i}(l,m)\leqslant 0)}]^2. \tag{7}$$

Of course this estimate can be accurate only if the camera offset has been subtracted carefully. The photon noise variance map is also estimated before the deconvolution, as

$$\sigma_{\text{ph}}^2(l, m) = \max[\mathbf{i}(l, m), 0]. \tag{8}$$

This estimate is quite precise for the bright regions in the image, where photon noise dominates. Its poor accuracy in the dark regions of the image is unimportant because in these regions the main contribution to the noise variance is given by the detector.

Note that if the image to be processed is actually obtained by subtraction of two images (e.g., in the infrared, an image of interest and a sky background), then the noise variance map of the difference image can be obtained by adding the individual variance maps estimated by means of Eq. (8) on each of the two images.

Finally, one could also contemplate estimating the photon noise variance $\sigma_{\text{ph}}^2(l, m)$ at each iteration from the current object estimate. This may make J_i a nonconvex function of $\mathbf{o}$, so we have discarded this possibility.

2. Object Prior

This section aims at deriving an object prior for objects that are either smooth or piecewise smooth, such as planets and natural or artificial satellites.

The choice of a Gaussian prior probability distribution for the object can be justified from an information theory standpoint as being the least informative, given the first two moments of the distribution. In this case, a reasonable model of the object's power spectral density (PSD) can be found[10] and used to derive the regularization criterion J_o, which is then quadratic. The model parameters can even be estimated from the image itself, as shown recently in the context of phase diversity.[19–21]

The disadvantage of a Gaussian prior (or equivalently of a quadratic regularization term), especially for objects with sharp edges such as asteroids or artificial satellites, is that it tends to oversmooth edges. A possible remedy is to use an edge-preserving prior that is quadratic for small gradients and linear for large ones.[22] The quadratic part ensures a good smoothing of the small gradients (i.e., of noise), and the linear behavior cancels the penalization of large gradients (i.e., of edges), as explained by Bouman and Sauer.[23] Such priors are called quadratic–linear, or L_2–L_1 for short.[24]

Here we use a function that is an isotropic version of the expression suggested by Rey[25] in the context of robust estimation, used by Brette and Idier[26] for image restoration, and recently applied to imaging through turbulence[27,28]:

$$J_o(\mathbf{o}) = \mu\delta^2 \sum_{l,m} \phi(\nabla\mathbf{o}(l, m)/\delta), \tag{9}$$

where

$$\phi(x) = |x| - \ln(1 + |x|) \tag{10}$$

and where $\nabla\mathbf{o}(l, m) = [\nabla_x\mathbf{o}(l, m)^2 + \nabla_y\mathbf{o}(l, m)^2]^{1/2}$, and $\nabla_x\mathbf{o}$ and $\nabla_y\mathbf{o}$ are the object finite-difference gradients along x and y, respectively. This functional J_o is indeed L_2–L_1 because $\phi(x) \approx x^2/2$ for x close to 0 and $\phi(x)/|x| \to 1$ for $x \to \pm\infty$. Thus parameter δ is a (soft) threshold, in the sense that J_o switches, at each pixel (l, m), between the quadratic and the linear behaviors depending on whether $\nabla\mathbf{o}(l, m)$ is smaller than or greater than δ.

The global factor μ and the threshold δ have to be adjusted according to the noise level and the structure of the object. These two hyperparameters currently have to be adjusted by hand. As a rule of thumb, a reasonable set of hyperparameters for L_2–L_1 regularization is to take $\mu \approx 1$ and δ to be on the order of the image gradient's norm, i.e., generally several times smaller than the object gradient's norm $\|\nabla\mathbf{o}\| = [\Sigma_{l,m}|\nabla\mathbf{o}(l, m)|^2]^{1/2}$ (because for high signal-to-noise ratios, the image is essentially a smoothed version of the object). This is supported by Künsch's findings in the context of noise removal with L_2–L_1 regularization.[29] When adjusting these hyperparameters, one should bear in mind that their sensitivity is logarithmic; i.e., one must increase or decrease them by a factor of 10 to see a notable difference. Additionally, we have noticed that convergence is somewhat faster when the inversion is more regularized, i.e., when μ or δ or both are large. This is not surprising, as the inverse problem is then better conditioned, and it suggests that one should begin with large values of the hyperparameters and make them decrease rather than the other way around. See, e.g., Ref. 12 for additional information on a working strategy of hyperparameter adjustment.

The functional J_o is strictly convex because $\phi''(x) = 1/(1 + |x|)^2 > 0$, and J_i^{mix} of Eq. (6) is convex because it is quadratic, so the global criterion $J = J_i^{\text{mix}} + J_o$ is strictly convex. This ensures uniqueness and stability of the solution with respect to noise and also justifies the use of a gradient-based method for the minimization.

The photometric quality of the restoration is an ever-present concern for astronomers, as the interpretation of the restored image may heavily depend on it. An appealing property of the prior of Eq. (9) is that it does not bias the global photometry of the restoration. Indeed, because it is a function of the local pixel value differences, this prior is insensitive to a global offset of the object. This is notably different from other priors such as the several variants of the entropy, which incorporate prior knowledge on the pixel values and thus bias the photometry.

If the object is a stellar field, then a stronger prior can be used, namely, the fact that the unknown object is a collection of Dirac delta functions. In this case, the unknown parameters are no longer a pixel map but the po-

sitions and magnitudes of each star.[11] The implementation of this alternative object prior in our restoration method, assuming that the number of stars is known, is hereafter called δ-MISTRAL. The case of a crowded stellar field with an unknown number of stars is a difficult problem of its own often called "deconvolution of spike trains." It has been addressed in many papers, including Refs. 30–33, and is outside the scope of this paper. See, e.g., Ref. 34 for a review on this subject.

B. Myopic Deconvolution

As mentioned in Section 2, the true PSF is seldom available. The deconvolution of turbulence-degraded images with an unknown PSF is a difficult subject. It has been tackled by many authors (see, e.g. Ref. 10 or Ref. 28 for a short review) and was first cast into a probabilistic framework, as a joint maximum-likelihood problem, by Holmes.[35] Considering the PSF to be completely unknown usually leads to unacceptable results, because estimating both the object and the PSF from a single image is a highly underdetermined problem. Typically, even when the positivity[36,37] of the object and the PSF is strictly enforced, the estimated PSF (or the estimated object) can be reduced to a Dirac delta function. It is thus necessary to regularize the problem by adding more constraints, both on the object (see Subsection 3.A.2) and on the PSF. In particular, the band-limitedness of the PSF has been found to be an effective one.[35,36,38] For short-exposure images, the fact that the optical PSF is completely described by a phase function over the aperture is a very effective constraint.[36,39] Unfortunately, for long-exposure images, this constraint is not fulfilled; for such images, Conan *et al.* have proposed a scheme called myopic deconvolution[10] that constrains the transfer function softly at all frequencies, which is more informative than the sole band-limitedness of the PSF. This scheme is adopted here; it consists in jointly estimating the PSF and the object in the same MAP framework. This joint MAP estimator is

$$\begin{aligned}[\hat{\mathbf{o}},\ \hat{\mathbf{h}}] &= \arg\max_{\mathbf{o},\mathbf{h}} p(\mathbf{o},\ \mathbf{h}|\mathbf{i}) \\ &= \arg\max_{\mathbf{o},\mathbf{h}} p(\mathbf{i}|\mathbf{o},\ \mathbf{h}) \times p(\mathbf{o}) \times p(\mathbf{h}) \\ &= \arg\min_{\mathbf{o},\mathbf{h}} [J_i(\mathbf{o},\ \mathbf{h}) + J_o(\mathbf{o}) + J_h(\mathbf{h})]. \quad (11)\end{aligned}$$

The myopic criterion contains the two terms of Eq. (4), the first one now being a function of $\mathbf{o}$ and of $\mathbf{h}$, plus an additional term $J_h = -\ln p(\mathbf{h})$ that accounts for the knowledge, although partial, available on the PSF. Such a three-term criterion has also been obtained in a deterministic approach.[40] The regularization term for the PSF can quite naturally be derived from our probabilistic approach. The PSF is considered to be a Gaussian stochastic process since it is the temporal average of a large number of short-exposure PSFs. Additionally assuming that the difference between the PSF and its mean is stationary, J_h is given by[10]:

$$J_h(\mathbf{h}) = \frac{1}{2}\sum_f \frac{|\tilde{\mathbf{h}}(f) - \tilde{\mathbf{h}}_\mathbf{m}(f)|^2}{S_h(f)}, \quad (12)$$

where $\tilde{\mathbf{h}}_\mathbf{m} = E[\tilde{\mathbf{h}}]$ is the mean transfer function and $S_h = E[|\tilde{\mathbf{h}}(f) - \tilde{\mathbf{h}}_\mathbf{m}(f)|^2]$ is the associated spatial PSD. J_h is interpretable as the energy of a set of springs (one per spatial frequency) that draw the transfer function toward its mean with a stiffness given by the PSD of the PSF, which characterizes the variability of the transfer function at each frequency. Such a regularization obviously ensures that the estimated transfer function is close to the mean transfer function with respect to error bars given by the PSD. The regularization in particular enforces a zero value for the estimate of $\tilde{\mathbf{h}}(f)$ above the cutoff of the telescope, because $S_h(f)$ is zero above the cutoff. This ensures the aforementioned band-limitedness of the PSF.

In practice, the mean PSF and its PSD are estimated by replacing, in their definitions, the expected values ($E[\ \cdot\ ]$) by an average on the different images recorded on an unresolved star. This star must be in a region where the seeing is the same as when observing the object. Additionally, the star flux should be chosen so that the wave-front sensing noise on the star is similar to the wave-front sensing noise on the object, the latter being a function of the object's spatial extent and flux.[41]

It is possible to estimate the PSF from the statistics of the wave-front sensing data,[14,42] which avoids the errors due to seeing fluctuations. The quantity estimated by this technique is actually the part of the *mean* PSF that is due to turbulence; the myopic approach is thus interesting in that it accounts for the PSF uncertainties due to constant aberration calibration errors,[11] residual speckle patterns because of the finite exposure time, and the wave-front sensing noise for faint stars.

Note that the new criterion is convex in $\mathbf{o}$ for a given $\mathbf{h}$ and convex in $\mathbf{h}$ for a given $\mathbf{o}$, but it is not necessarily convex on the whole parameter space. However, using reasonable starting points (see Section 4), we did not encounter the minimization problems associated with nonconvexity.

4. IMPLEMENTATION ISSUES

A. Minimization Method

The criterion of Eq. (11) is minimized numerically to obtain the joint MAP estimate for the object $\mathbf{o}$ and the PSF $\mathbf{h}$. The minimization is performed by a conjugate-gradient method,[43] which is usually recognized to be faster than expectation-maximization-based algorithms. The convergence of the conjugate-gradient method to a stationary point (in practice, to a local minimum) is guaranteed[44] because the criterion is continuously differentiable. We have found that the convergence is faster if the descent direction is re-initialized regularly; this can be attributed to the fact that the criterion to be minimized is not quadratic. This modified version of the conjugate gradient is known as the partial conjugate-gradient method and has similar convergence properties (see Sec. 8.5 of Ref. 45).

The simplest way to organize the unknowns for the minimization is to stack the object and the PSF together into a vector and to run the conjugate-gradient routine on this variable. Yet this can be slow, as the gradients of the

criterion with respect to the object and to the PSF may have different orders of magnitude. We have found that the minimization is speeded up by splitting it into two blocks and alternating between minimizations on the object for the current PSF estimate and minimizations on the PSF for the current object estimate. Additionally, for a given (current) object, the criterion of Eq. (11) is quadratic with respect to the PSF, so its minimum in **h**, without the positivity constraint, is analytical. This analytical expression can still be used as a starting point for the estimation of **h** if one wants to enforce positivity of the PSF.

The minimization starts by estimating the object for a fixed PSF taken as the mean PSF. The initial guess for the object is either the image itself or a Wiener-filtered version of the image. The minimization is not stopped by hand but rather when the estimated object and PSF no longer evolve (i.e., when their evolution from one iteration to the next is close to machine precision).

B. Positivity Constraint

The object intensity map is a set of positive values, which is important *a priori* information. One should therefore enforce a positivity constraint on the object. This constraint can be implemented in various ways,[46] such as criterion minimization under the positivity constraint, reparameterization of the object, or explicit modification of the *a priori* probability distribution (e.g., addition of an entropic term). The first two methods can actually be interpreted as an implicit modification of the *a priori* distribution that gives a zero probability to objects having negative pixel values. Note that with some expectation-maximization-based algorithms such as the Richardson–Lucy algorithm, the positivity constraint is automatically satisfied provided that the initial guess is positive.

The addition of an entropic term notably slows down the minimization; additionally, it degrades the photometric quality of the restored image as mentioned above. The reparameterization is easy to implement, but the only one we found that does not notably slow down the minimization is[47] $\mathbf{o}(l, m) = \mathbf{a}(l, m)^2$, which induces local minima because it is not monotonic. We have found that the best way to ensure positivity, with respect both to speed and to not introducing local minima, is to directly minimize the criterion under this constraint. We do so by means of the projected gradient, as proposed in image processing by Commenges[48] and by Nakamura *et al.*[49]

5. VALIDATION ON SIMULATED DATA

This section successively validates the contribution of the various components of our restoration method to the quality of the restored image, by means of simulations. These components are the noise model, the positivity, the edge-preserving object prior, and the myopic capability. To have a realistic PSF and PSF variability, we use as PSFs five experimental NAOS–CONICA[50] images of an unresolved bright star recorded in the Brγ narrow band (wavelength $\lambda = 2.166\ \mu$m). They are shown in Fig. 1. Their Strehl ratios range from 52% to 66%, and the Strehl ratio fluctuation is due to seeing variations. In all subsections but Subsection 5.D, the PSF is assumed to be known.

Two types of objects are used: a planetary-type object (synthetic asteroid of uniform level with a 10% brighter broad feature and three 30% brighter spots, surrounded by a few stars), and a galaxy (scaled image of M51).

The images are obtained by convolution of these objects with a PSF (the fourth of the PSFs shown in Fig. 1) and contamination by noise. The noise is the combination of photon noise (Poisson statistics with a total flux of 10^7 photons) and detector noise [stationary Gaussian statistics with a standard deviation of 10 photoelectrons/pixel (ph/pix)].

Figure 2 shows the objects and the simulated noisy images. The ideal, i.e., noiseless diffraction-limited, images are also shown for comparison.

A. Effect of the Noise Model

The restored object minimizes Eq. (4) with J_o being the quadratic regularization derived from the Gaussian prior used in Ref. 10. Figure 3 shows the best restorations obtained for each of two white-noise models when the global hyperparameter μ is varied. These models are the simple stationary model, which leads to the least-squares criterion J_i^{swG} mentioned in Subsection 3.A.1, and the nonstationary model J_i^{mix} of Eq. (6), which accounts for both photon noise and detector noise. The root-mean-square error is slightly smaller for the finer noise model (2052 ph/pix) than for the simple one (2115 ph/pix). This error is computed as the mean square difference between the restoration and the true object on all pixels where the object's value is nonzero, so it is indeed indicative of the restoration quality of the object rather than of the background. Visually, the presence of the star on the right of

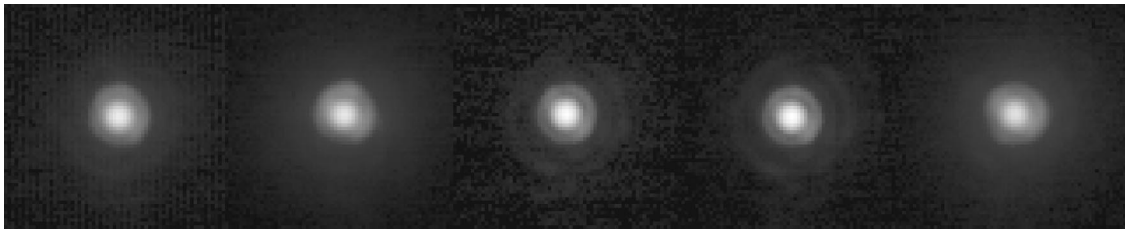

Fig. 1. Five experimental VLT-NAOS-CONICA images of an unresolved bright star recorded on Sep. 29, 2002, at 20:58 UT in the Brγ narrow band and used in the simulations (wavelength $\lambda = 2.166\ \mu$m, exposure time 2 s). The fourth one is used as the true PSF. The estimated Strehl ratios are 57%, 52%, 64%, 66%, and 58%. The corresponding Fried parameters are $r_0 = 17.5$, 15.6, 20.7, 21.0 and 17.0 cm.

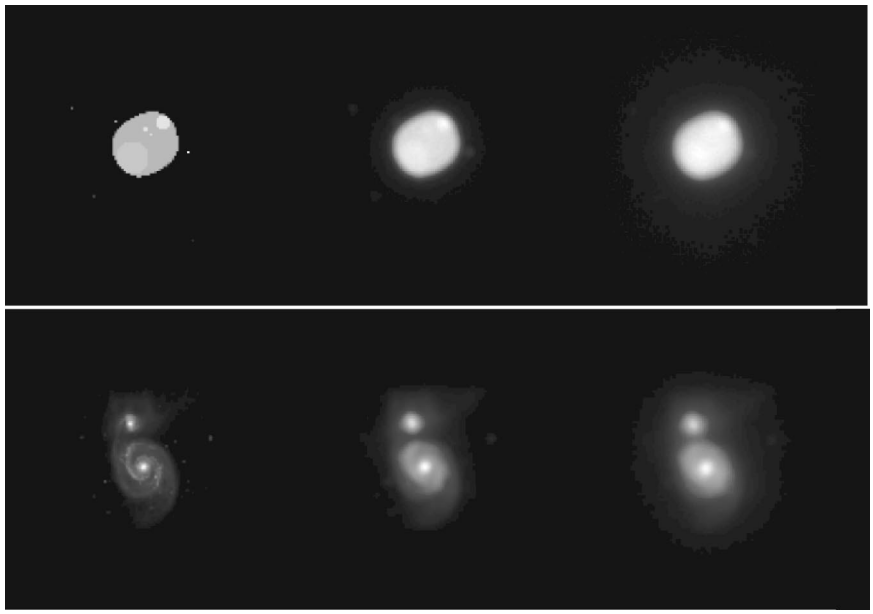

Fig. 2. From left to right: original object used for the simulation, noiseless image by a perfect diffraction-limited telescope (for comparison), and simulated image obtained by adding noise to the convolution of the object by the PSF (the fourth of the PSFs shown in Fig. 1). Top, asteroid; bottom, galaxy.

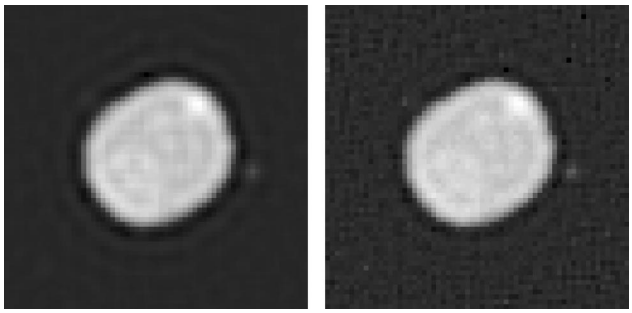

Fig. 3. Best restorations of the asteroid obtained with quadratic regularization for the two noise models, without a positivity constraint. Left, stationary model; right, nonstationary model, which accounts for both photon noise and detector noise. Restoration errors are 2115 and 2052 ph/pix, respectively. These restored images are zoomed by a factor of two for better visualization.

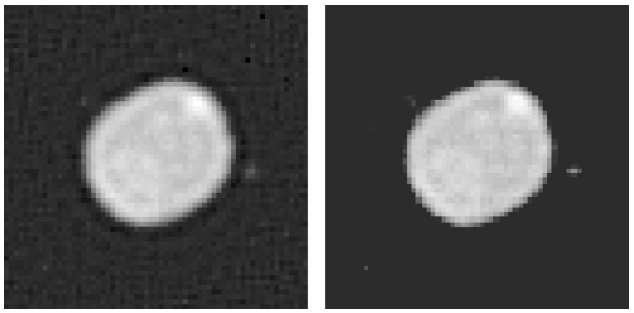

Fig. 4. Restorations of the asteroid obtained with quadratic regularization and the nonstationary noise model, without (left) and with (right) the positivity constraint. Restoration errors are 2052 and 1764 ph/pix, respectively. These restored images are zoomed by a factor of 2 for better visualization.

the asteroid is more obvious with the finer model, which is the one used from now on.

B. Effect of the Positivity Constraint

The influence of the positivity constraint is illustrated on the asteroid case in Fig. 4. It is implemented through projection, as discussed in Subsection 4.B. This constraint helps reduce noise and ringing in the dark regions of the image, i.e., where it is actually enforced. Indeed, the root-mean-square error drops from 2052 to 1764 ph/pix; this constraint will thus be used in all the following restorations.

Yet, some ringing remains inside the object because of its sharp edges and the use of a quadratic regularization; indeed, quadratic regularization precludes spectral extrapolation and thus can produce a restored object with a sharp cutoff in Fourier space. In the object space, this sharp cutoff takes the form of ringing, akin to Gibbs oscillations.[51] Such artifacts prevent any astrophysical interpretation that would rely on precise photometry.

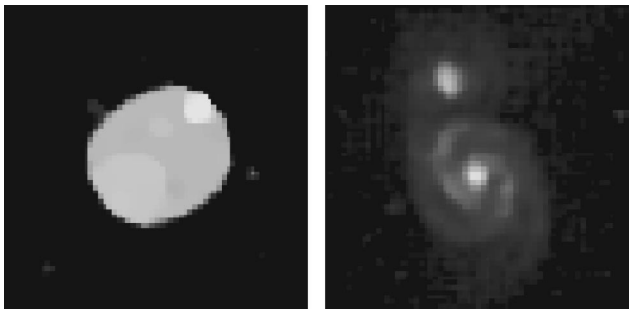

Fig. 5. Restorations obtained with the edge-preserving prior, the nonstationary noise model, and the positivity constraint for the best values of the hyperparameters. Restoration errors are 1201 ph/pix for the asteroid (left) and 985 ph/pix for the galaxy (right). These restored images are zoomed by a factor of 2 for better visualization.

C. Effect of the Edge-Preserving Object Prior

Figure 5 shows the restoration of the asteroid and of the galaxy with the edge-preserving prior of Eq. (9). They are obtained with $(\delta, \mu) = (0.03, 30)$ and $(30, 0.03)$, respectively. The restoration errors are, respectively, 1201

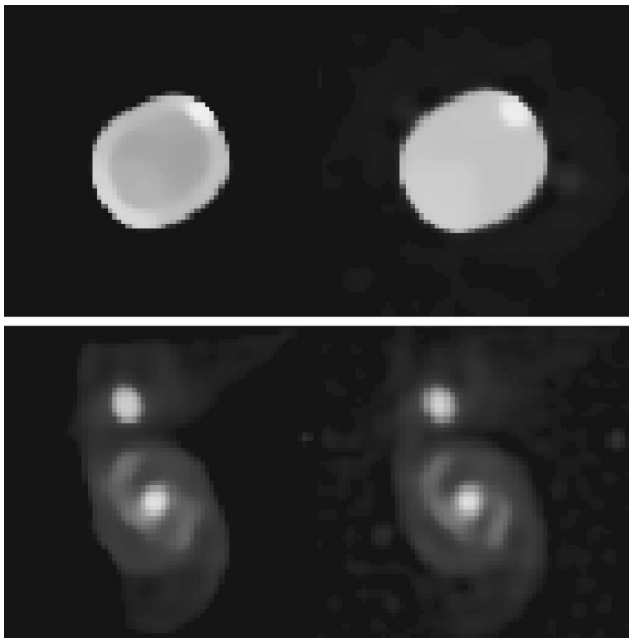

Fig. 6. Classical deconvolution using the mean PSF as the true one (left); myopic deconvolution (right). Restoration errors are 5139 and 2333 ph/pix, respectively, for the asteroid (top) and 1671 and 1365 ph/pix for the galaxy (bottom).

and 985 ph/pix. The enhancement of the photometric quality of the L_2–L_1 restoration of the asteroid, with respect to the quadratic restoration of Fig. 4, is obvious: The 10% brighter broad feature and the largest of the three 30% brighter spots are visible, and the piecewise uniformity of the asteroid is respected.

D. Effect of the Myopic Capability

This subsection assumes that the true PSF is unknown and that we instead have five noisy PSFs taken shortly before or after the object of interest. These are the five images of a nearby star shown in Fig. 1. We thus use the myopic scheme described in Subsection 3.B, which is capable of estimating the PSF and the object simultaneously. We use the edge-preserving prior of Eq. (9) and the fine noise model of Eq. (6). The mean PSF and the PSD of the PSF are estimated by replacing, in their definitions, the expected values ($E[\,\cdot\,]$) by an average on the five images. The quality of the restoration can be favorably compared with that of a "classical" (i.e., with known PSF) deconvolution by using the mean PSF: for the asteroid, the latter deconvolution gives an error of 5139 ph/pix, whereas the myopic deconvolution gives an error of 2333 ph/pix. For the galaxy, these restoration errors are 1671 and 1365 ph/pix, respectively. Figure 6 shows the restored asteroid and galaxy for the two restoration methods. As expected, the myopic deconvolution performs better than the classical deconvolution with mean PSF because the former does not assume erroneously that the PSF is known, but not as well as the classical deconvolution with the true PSF (see Fig. 5).

6. DECONVOLUTION OF EXPERIMENTAL DATA

This section presents results obtained on different types of AO systems (BOA, NAOS, HOKUPA'A, ADONIS, PUEO, Keck-AO) and different kinds of astronomical objects (planetary objects, pointlike objects, etc). The average PSF and the PSD of the PSF is computed from a set of images of a nearby star recorded after (and also before, whenever possible) the object of interest. For each of these examples, astrophysical results have been derived from the deconvolved images and have lead to scientific publications.

A. Planetary Objects

1. Ganymede Observed with BOA

Ganymede is the biggest moon of Jupiter (visual magnitude $M_v = 4.6$, diameter approximately 1.7 arcsec). It was observed by the 1.52-m telescope of Observatoire de Haute Provence by ONERA's AO bench called BOA (for Banc d'Optique Adaptative) on September 28, 1997.[52,53] The seeing conditions were particularly severe: $D/r_o \approx 23$ at the imaging wavelength 0.85 μm. The object itself is used for the wave-front sensing. The corrected image (100 s exposure time) is shown in Fig. 7(a) and does not exhibit any detail (the Strehl ratio is approximately 5%). The field of view is 3.80 arcsec. The estimated total flux is approximately 8×10^7 photons. The star θ Cap ($M_v = 4.1$), located 1.5 deg away from Ganymede, was then observed to provide a PSF calibration. A neutral density, i.e., a light attenuator that is not chromatic, was used to have approximately the same wave-front sensing conditions. The PSD of the PSF and the mean PSF were estimated from a series of 50 images recorded with an exposure time of 1 s. The difference in exposure times between the reference star and Ganymede was accounted for in the PSD computation.[10] The MISTRAL de-

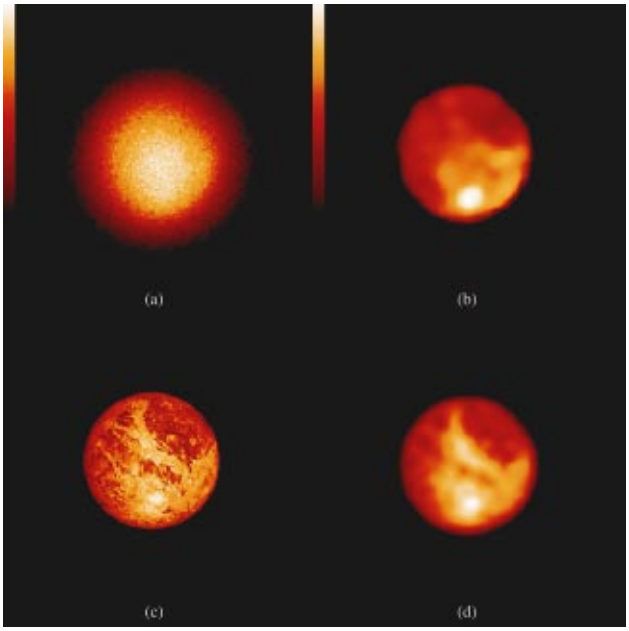

Fig. 7. (a) image of Ganymede with ONERA's AO bench at the 1.52-m telescope of Observatoire de Haute Provence on 1997/09/28, 20:18 UT. (b) MISTRAL deconvolution. (c) Synthesized image obtained by mapping broadband probe images of NASA's data base into a view of Ganymede seen from Earth at the time (a) was taken (courtesy NASA/JPL/Caltech, see http://space.jpl.nasa.gov/). (d) Same synthesized image convolved with the Airy disk of a 1.52-m telescope, for comparison with the deconvolved image.

convolution is shown on Fig. 7(b). Although a probe passing by Jupiter obviously exhibits a better resolution than a 1.52-m telescope on the ground, many features of Ganymede (various dark areas, bright spot) are visible in the deconvolved AO-corrected image and can be compared with the NASA/JPL high-resolution image [Fig. 7(c)]. The latter image was synthesized by mapping broadband probe images of NASA/JPL's database into a view of Ganymede seen from Earth at the time Fig. 7(a) was taken (see the solar system simulator at http://space.jpl.nasa.gov/). A fairer comparison can be done between the MISTRAL deconvolution and the image of Fig. 7(c) convolved with the Airy pattern of a 1.52-m telescope; the latter image is shown on Fig. 7(d).

2. Io Observed with Keck-AO

Io, the innermost Galilean satellite of Jupiter (with angular size of 1.2 arcsec) was observed in near IR in February 2001 from the 10-m Keck II telescope with use of its AO system. After deconvolution with MISTRAL, the resolution, approximately 100 km on Io's disk, is comparable with the best Galileo/NIMS (Near Infrared Mapping Spectrometer) resolution for global imaging and allows, for the first time, investigation of the very nature of individual eruptions[54] (see Figs. 8 and 9). On February 19, two volcanos, Amirani and Tvshatar, with temperatures differing from the Galileo observations, were observed. On February 20, a slight brightening near the Surt volcano was detected that turned into an extremely bright volcanic outburst two days later. Thanks to the quality of the photometric restitution obtained with MISTRAL,[55] these outburst data have been fitted with a silicate cooling model, which indicates that this is a highly vigorous eruption with a highly dynamic emplacement mechanism, akin to fire fountaining. Its integrated thermal output was close to the total estimated output of Io, making this the largest Ionian thermal outburst yet witnessed.

3. Io Observed with NAOS

Io was observed on December 5, 2001, with the recently commissioned VLT/NAOS AO system[50,56] and its infrared camera CONICA.[57] The Strehl ratio on this Bracket-γ (2.166 μm) observation is estimated to be 35%. This wavelength range mainly gives information about reflected sunlight modulated by various surface features. The image deconvolved with MISTRAL is shown in Fig. 10. Dark caldera, such as Pele and Pillan patera, are visible in the southeast area of the disk. The low-albedo area that is at the North of the center of the disk corresponds to Lei–Kung fluctus, a lava flow field. No high-temperature volcanic hot spot was detected during this observing night. Ground-based monitoring programs us-

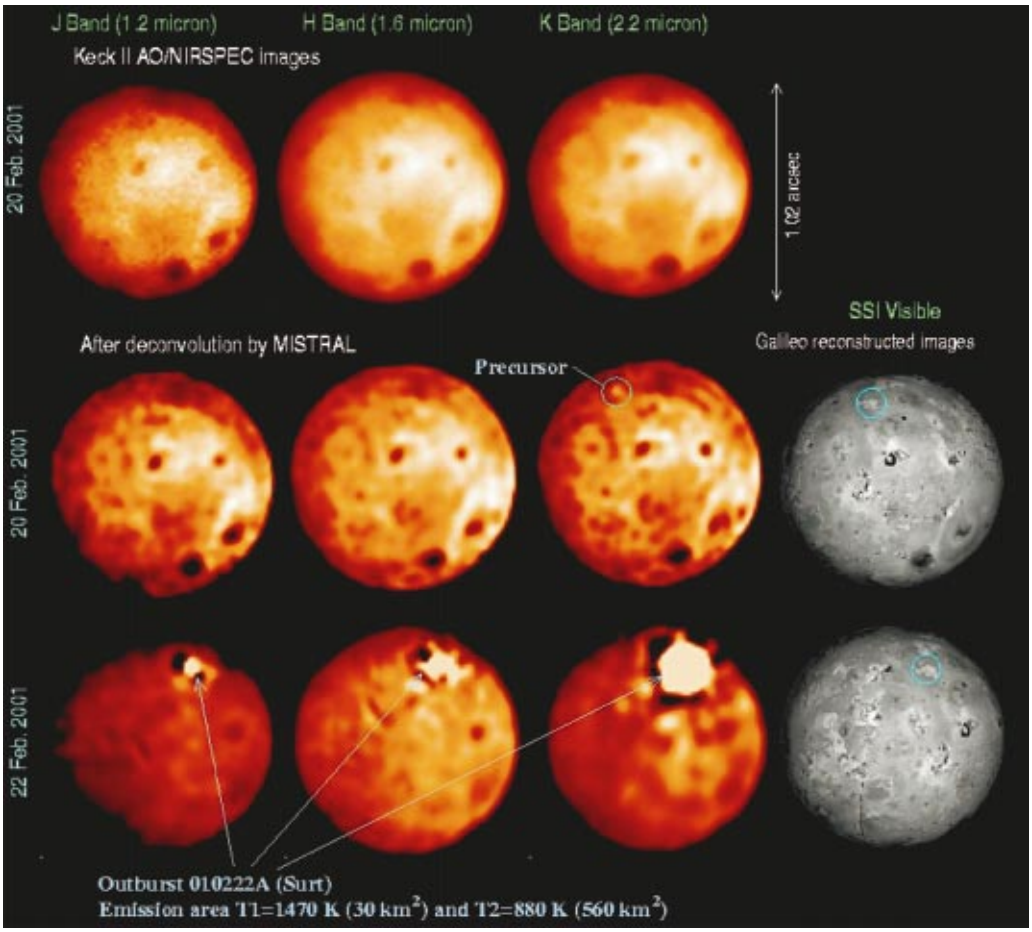

Fig. 8. Jupiter-facing hemisphere of Io observed with the Keck AO system in J, H, and K band (from left to right). The basic preprocessed images from February 20, 2001, are displayed on the first row. The second row corresponds to the same images after deconvolution. Albedo features, comparable with the 20-km resolution reconstructed Galileo/SSI image (right column) are easily detected. The last row shows the February 22, 2001, images, which are dominated by the presence of the Surt outburst.

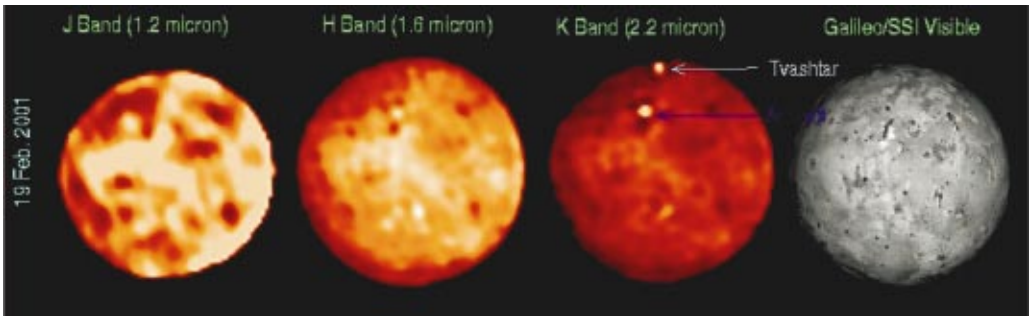

Fig. 9. Io observed by the Keck from February 19, 2001, and deconvolved with MISTRAL. Two hot spots, corresponding to Tvashtar (north) and Amirani, are clearly detected in the H and K bands. The bad seeing conditions of this observation induced very poor AO correction in the J band, which explains the poor restitution quality in the J band.

ing AO systems on 8-m–10-m-class telescopes will help astronomers characterize the time evolution of Io's volcanic activity, including the frequency, spatial distribution, and temperature of hot spots and surface changes.[58,59] Indeed, with the Galileo mission coming to an end, the future monitoring of Io's volcanism lies in the hands of terrestrial observers.

4. Neptune Observed with HOKUPA'A

The 36-actuator curvature AO system called HOKUPA'A was used to observe Neptune at the Canada–France–Hawaii Telescope both in November 1997 and in July 1998. It produced the first sharp infrared images of Neptune. These images show the fine structures of its cloud bands with high contrast, allowing the details of Neptune's atmospheric activity to be observed from the ground for the first time.[60] Figure 11 shows images of Neptune obtained on July 6, 1998 in a methane absorption band (1.72 μm) and deconvolved with MISTRAL. At this wavelength Neptune's atmosphere is very dark, and high altitude clouds appear with a high contrast. The top three images are individual 600-s exposures taken at the time indicated above each image. Note how the fine structure in the cloud bands can be followed from one frame to another as the planet rotates. The upper left and right images have been numerically rotated about Neptune's rotation axis to match the central image and added to it to form the bottom left image, thus improving the signal-to-noise ratio. The bottom right image is the same as the bottom left one except for its color table, which better shows the low-light levels. The periodic pattern of bright dots seen just above the southernmost cloud band (at the bottom of each image) is particularly remarkable. Such a regular pattern of small clouds has never before been observed on Neptune and may be indicative of gravity waves in Neptune's atmosphere.

5. Uranian System Observed with ADONIS

MISTRAL has been applied to infrared images of Uranus acquired on May 2, 1999 with the ADONIS AO system. The deconvolved images in the J and H bands exhibit structures on the planet (bright polar haze).[61] When looking at low intensity levels (see Fig. 12), one can also see the structure of the Epsilon ring and of the innermost rings, as well as very faint satellites discovered by Voyager 2 in 1986 and never reobserved since.

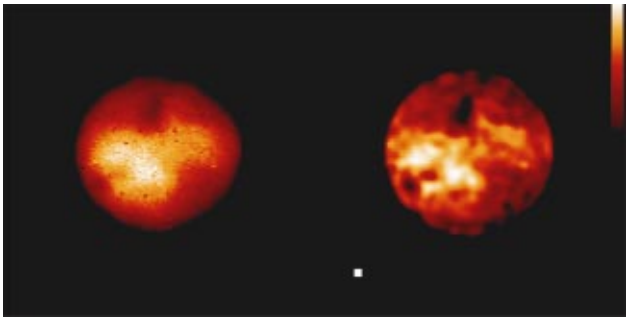

Fig. 10. Left: Io observed with NAOS–CONICA on December 5th, 2001 (7:14:59 UTC), in the Brγ band (2.166 μm); north is up and east is left. The object itself is used for the wave-front sensing. The camera pixel scale is 13.25 mas. The seeing was 0.9 arcsec, and the estimated Strehl ratio is 35%. Right, deconvolution using MISTRAL. The two images are given in the same linear color scale. The white square represents the telescope diffraction limit at the observing wavelength.

B. Disklike Objects: MBM 12 Association Observed with Pueo

In the younger association MBM 12, seven binaries and a quadruple system including a protoplanetary disk have recently been detected and deconvolved.[62] For the young protoplanetary disk LkHα 263 C seen almost perfectly edge-on, MISTRAL was applied to recover the maximum spatial information possible (see Fig. 13). The deconvolved images were then compared with synthetic images of a disk model so as to extract structural parameters such as outer radius, dust mass, and inclination.[62]

C. Pointlike Objects

1. Capricornus Association Observed with ADONIS

The young, nearby stellar associations are ideal laboratories to study the formation and evolution of circumstellar disks, brown dwarfs, and planets around solar-type stars. Owing to their proximity (closer than 100 pc), small separations can be reached to explore the faint circumstellar environment of such associations. In the Capricornus association (distance 48 pc; age less than 30 Myr), the source HD 199143 has been previously resolved as a binary system.[63] The strong IR color ($J - K = 1.37$) of

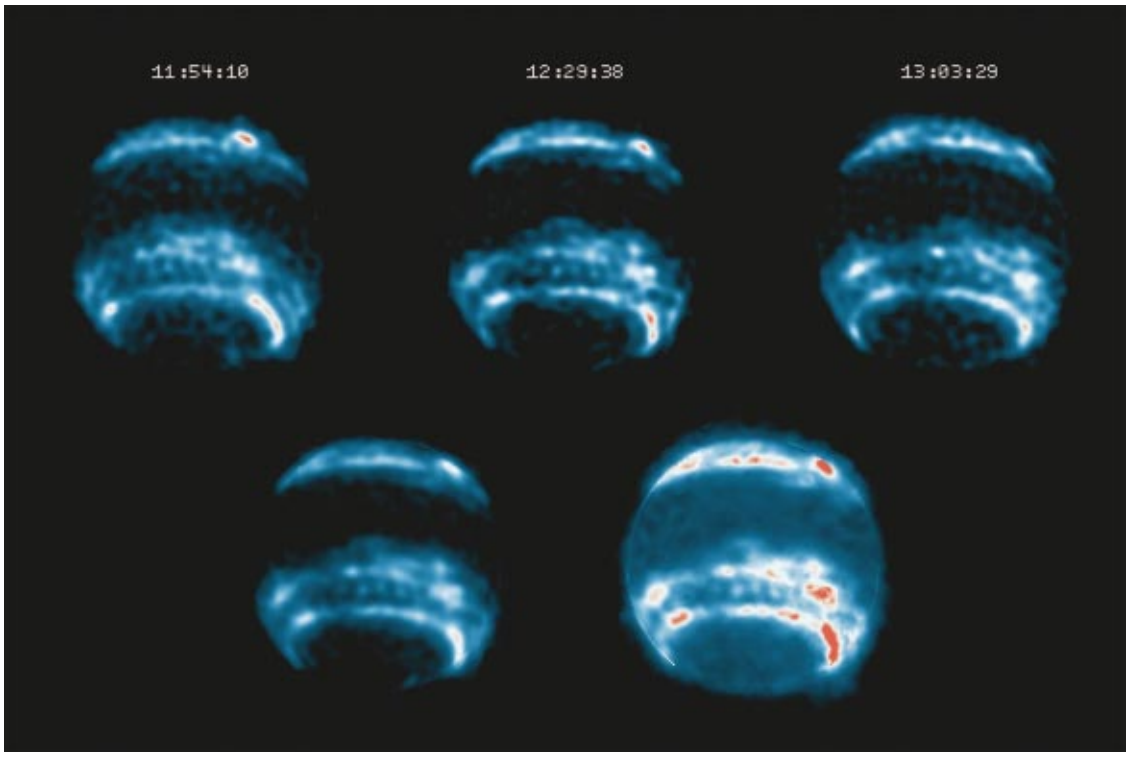

Fig. 11. False-color images of Neptune obtain at the Canada–France–Hawaii Telescope with the HOKUPA'A AO system on July 6, 1998, in a methane absorption band (1.72 μm) and deconvolved by MISTRAL. The object itself is used for the wave-front sensing. The top three images are individual 600-s exposures taken at 11:54:10, 12:29:38, and 13:03:29 UT time. The left and right images have been numerically rotated about Neptune's rotation axis to match the central image and co-added to it to form the bottom images, thus improving the signal-to-noise ratio. The color scale in the bottom right image shows the fainter details.

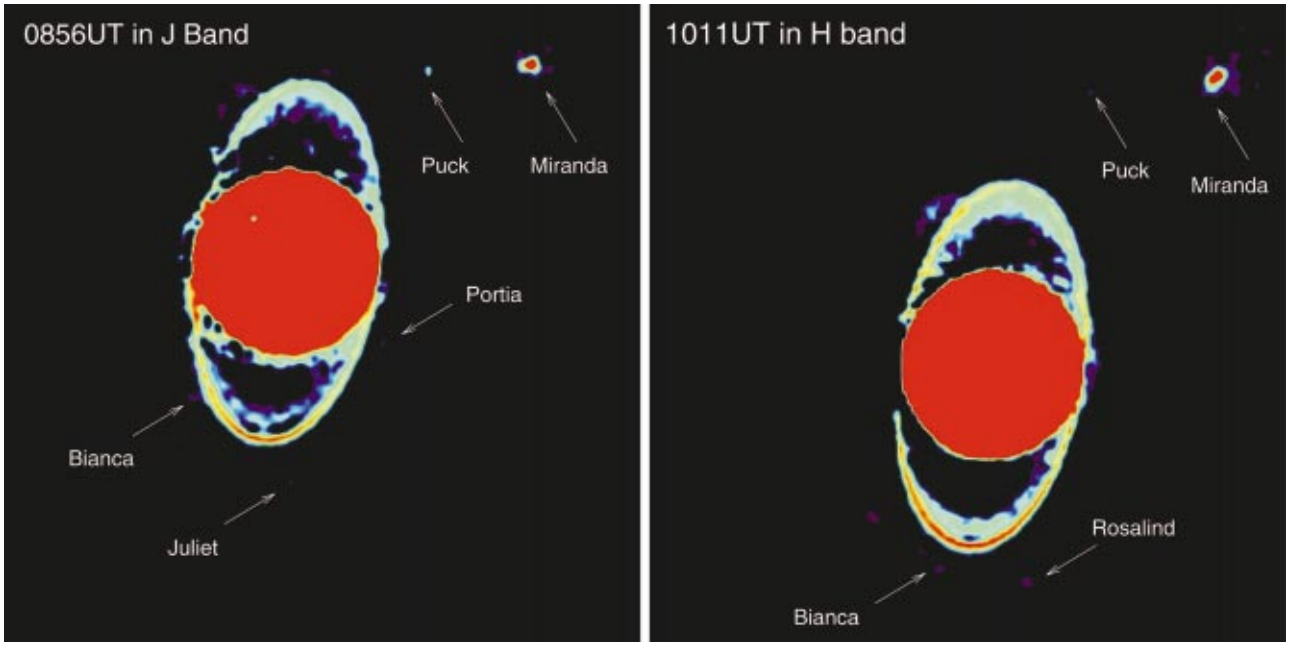

Fig. 12. Logarithmic display of the images restored by MISTRAL; north is up and east is left. The chosen color scale saturates the high levels so as to make visible the faint details. Innermost rings and faintest satellites, first observed with Voyager in 1986, are also detected.

the companion had been estimated from an image deconvolved with IDAC (Iterative Deconvolution Algorithm in C)[38] and attributed to the presence of a "circumsecondary" disk. New observations of Chauvin *et al.*, after deconvolution by δ-MISTRAL (see an example of deconvolution with MISTRAL in the J band in Fig. 14), did not confirm the photometry in the J band of HD 199143 B. Instead, these new results showed that no disk is needed to explain the re-estimated IR color ($J - K = 0.81$) of HD 199143 B, now interpreted as a late M2 dwarf.[64]

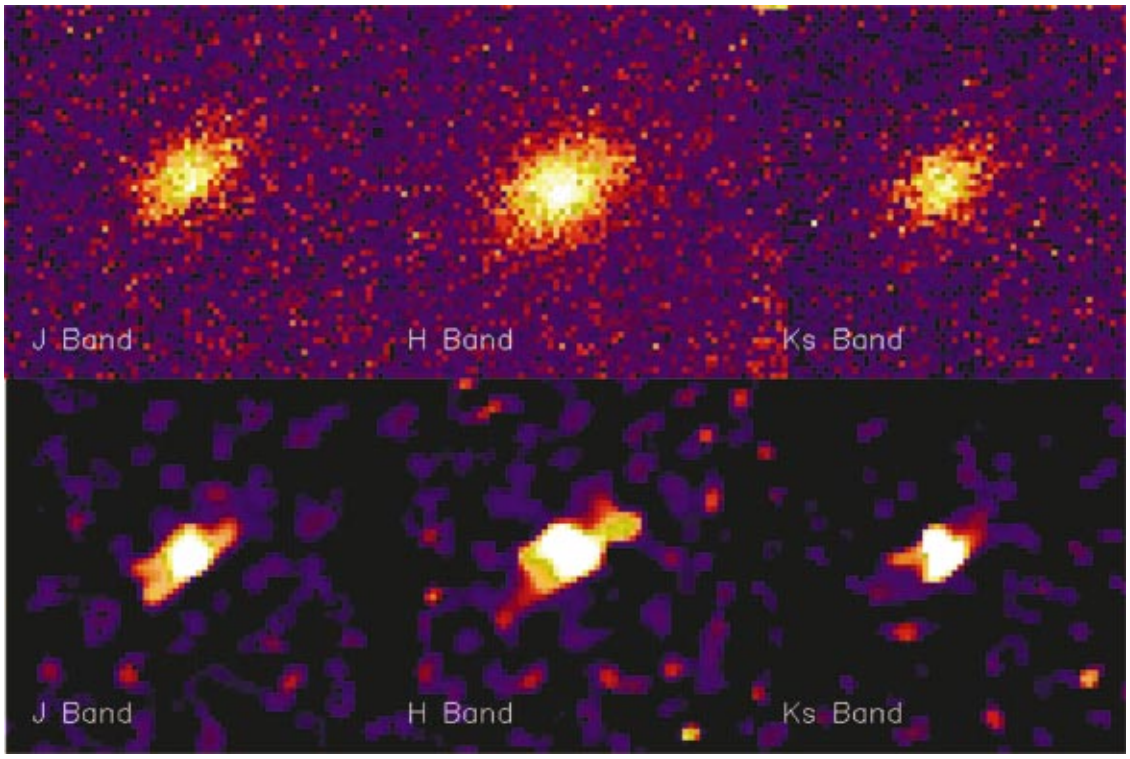

Fig. 13. Top row, raw images of the circumstellar disk surrounding LkHα 263 C in J, H, and Ks (from left to right). Bottom row, corresponding deconvolved images. On all images the field of view is 2.2 arcsec, with north up and east to the left.

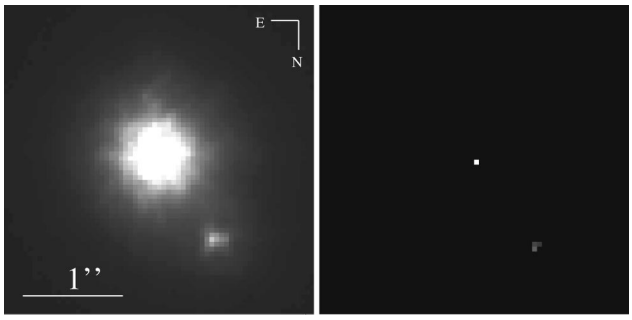

Fig. 14. Left, ADONIS image in the J band of HD 199143 A and B. The object itself is used for the wave-front sensing. Right, resulting image obtained with MISTRAL.

2. GJ263 Observed with NAOS

Figure 15 shows how diffraction-limited imaging with NAOS–CONICA at a wavelength of 1.257 μm shows the individual components of the close binary star GJ 263. The angular distance between the two stars is only 0.040 arcsec. Spatially resolved observations combined with precise photometric deconvolution of binary stars like this one will allow the determination of orbital parameters and ultimately of the masses of the individual binary star components.

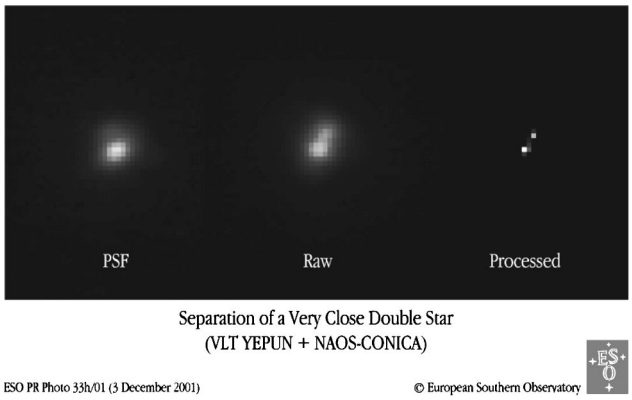

Fig. 15. NAOS–CONICA image of the double star GJ 263; the angular distance between the two components is 0.040 arcsec. The raw image, as directly recorded by CONICA, is shown in the middle, with a MISTRAL deconvolved version to the right. The recorded PSF is shown to the left. The object itself was used for the wave-front sensing. The C50S camera (0.01325 arcsec/pixel) was used with an FeII filter at the near-infrared wavelength 1.257 μm. The exposure time was 10 s. (See http://www.eso.org/outreach/press-rel/pr-2001/pr-25-01.html for more details).

D. Other Objects and Other Adaptive Optics Systems

A nonexhaustive list of astronomical images taken on various systems and deconvolved with MISTRAL is presented below with their corresponding publications.

- Titan observed with PUEO[65] and with Keck-AO[66]: detection of albedo surface features.
- Tucana–Horologium association observed with ADONIS[67]: precise photometry on several binaries.
- The main belt asteroid 216-Kleopatra observed with ADONIS[68]: bifurcated shapes, density, and origin.
- The main belt asteroid Vesta observed with Keck-AO: shape, mineralogy, etc.

7. CONCLUSION AND PERSPECTIVES

A deconvolution method has been derived in a Bayesian framework. Its three main components are a fine noise

model, a PSF estimation capability, and a carefully designed object regularization term. The nonstationary noise model accounts for both photonic and detector noise and yields a large dynamic range in the restored images. Additionally, this method reckons with the usually imperfect knowledge of the PSF by estimating the PSF simultaneously with the object under soft constraints that embody our uncertainty about the PSF. Finally, this method comprises a regularization term that is appropriate for a wide class of objects, namely, objects that are a mix of sharp edges and smooth areas. This regularization does not bias the photometry and can restore sharp edges without ringing effects. The implementation of this method, called MISTRAL, allows a positivity constraint to be enforced both on the object and on the PSF.

The contributions of the different components of this method to the overall quality of the restoration have been validated by simulations. The effectiveness of MISTRAL has been illustrated by several results on experimental and scientific data taken on various AO systems and telescopes. Additionally, this method has already been successfully employed in a number of astronomical publications to derive astrophysical results.

Future work should include the automatic tuning of the hyperparameters. The deconvolution of images larger than the isoplanatic patch also deserves further study. At least when the PSF is known, the result of the use of MISTRAL "as is" on such data can be predicted. Indeed, it has been shown that for AO-corrected images, the PSF within an angular patch away from the guide star is the on-axis PSF convolved with an anisoplanatism PSF,[69] which is a delta function on axis and widens as the considered patch direction gets farther from the guide star. Hence MISTRAL should be able to deconvolve the image from the on-axis PSF and restore an object smoothed only by this anisoplanatism PSF.

Finally, integrating the PSF out of the problem rather than estimating it jointly with the object should also be studied. Indeed, the reverse operation, i.e., integrating the object out of the problem when estimating the PSF of an instrument, has already been proven to be a successful approach in the context of phase diversity, since it offers robustness to noise and should asymptotically remove the local minima associated with the joint estimation.[20,21]

ACKNOWLEDGMENTS

We are grateful to our colleagues of the High-Resolution Imaging team at ONERA for making the Banc d'Optique Adaptative happen as well as for many fruitful discussions. We warmly thank all the astronomers who participated in the data reduction and used the deconvolved images for their astrophysical interpretations, in particular Franck Marchis, Gaël Chauvin and the NAOS–CONICA team, François and Claude Roddier, Christophe Dumas, and Athena Coustenis. We acknowledge the referees for their most careful reviews and constructive comments.

Corresponding author Laurent Mugnier can be reached at Laurent.Mugnier@onera.fr.

REFERENCES

1. J. W. Hardy, J. E. Lefevbre, and C. L. Koliopoulos, "Real time atmospheric compensation," J. Opt. Soc. Am. **67**, 360–369 (1977).
2. G. Rousset, J.-C. Fontanella, P. Kern, P. Gigan, F. Rigaut, P. Léna, C. Boyer, P. Jagourel, J.-P. Gaffard, and F. Merkle, "First diffraction-limited astronomical images with adaptive optics," Astron. Astrophys. **230**, 29–32 (1990).
3. F. Roddier, ed., *Adaptive Optics in Astronomy* (Cambridge U. Press, Cambridge, UK, 1999).
4. F. Rigaut, G. Rousset, P. Kern, J.-C. Fontanella, J.-P. Gaffard, F. Merkle, and P. Léna, "Adaptive optics on a 3.6-m telescope: results and performance," Astron. Astrophys. **250**, 280–290 (1991).
5. M. C. Roggemann, "Limited degree-of-freedom adaptive optics and image reconstruction," Appl. Opt. **30**, 4227–4233 (1991).
6. J. M. Conan, P. Y. Madec, and G. Rousset, "Image formation in adaptive optics partial correction," in *Active and Adaptive Optics*, F. Merkle, ed., ESO Conference and Workshop Proceedings (Garching bei München, Germany, 1994), pp. 181–186.
7. J.-M. Conan, "Étude de la correction partielle en optique adaptative," Ph.D. thesis (Université Paris XI Orsay, Orsay, France, 1994).
8. G. Demoment, "Image reconstruction and restoration: overview of common estimation structures and problems," IEEE Trans. Acoust. Speech Signal Process. **37**, 2024–2036 (1989).
9. J. Idier, ed., *Approche bayésienne pour les problèmes inverses* (Hermès, Paris, 2001).
10. J.-M. Conan, L. M. Mugnier, T. Fusco, V. Michau, and G. Rousset, "Myopic deconvolution of adaptive optics images by use of object and point-spread function power spectra," Appl. Opt. **37**, 4614–4622 (1998).
11. T. Fusco, J.-P. Véran, J.-M. Conan, and L. Mugnier, "Myopic deconvolution method for adaptive optics images of stellar fields," Astron. Astrophys. Suppl. Ser. **134**, 1–10 (1999).
12. A. D. Storrs, C. Dunne, J.-M. Conan, L. Mugnier, B. P. Weiss, and B. Zellner, "A closer look at main belt asteroids 1: WF/PC images," Icarus (to be published).
13. D. Gratadour, L. M. Mugnier, and D. Rouan, "Image centering with a maximum likelihood estimator: application to infrared astronomical imaging," in *ADASS XIII*, F. Ochsenbein, M. Allen, and D. Egret, eds., Astron. Soc. Pacific Conf. Series 30 (Publications of the Astronomical Society of the Pacific, San Francisco, Calif., 2004); manuscript available from the authors, Damien.Gratadour@onera.fr.
14. J.-P. Véran, F. Rigaut, H. Maitre, and D. Rouan, "Estimation of the adaptive optics long-exposure point-spread function using control loop data," J. Opt. Soc. Am. A **14**, 3057–3069 (1997).
15. A. Blanc, L. M. Mugnier, and J. Idier, "Marginal estimation of aberrations and image restoration by use of phase diversity," J. Opt. Soc. Am. A **20**, 1035–1045 (2003).
16. M. Hartung, A. Blanc, T. Fusco, F. Lacombe, L. M. Mugnier, G. Rousset, and R. Lenzen, "Calibration of NAOS and CONICA static aberrations. Experimental results," Astron. Astrophys. **399**, 385–394 (2003).
17. W. H. Richardson, "Bayesian-based iterative method of image restoration," J. Opt. Soc. Am. **62**, 55–59 (1972).
18. J. Nunez and J. Llacer, "A general Bayesian image reconstruction algorithm with entropy prior: preliminary application to HST data," Publ. Astron. Soc. Pac. **105**, 1192–1208 (1993).
19. A. Blanc, J. Idier, and L. M. Mugnier, "Novel estimator for the aberrations of a space telescope by phase diversity," in *UV, Optical, and IR Space Telescopes and Instruments*, J. B. Breckinridge and P. Jakobsen, eds., Proc. SPIE **4013**, 728–736 (2000).
20. A. Blanc, "Identification de réponse impulsionnelle et restauration d'images: apports de la diversité de phase," Ph.D. thesis (Université Paris XI Orsay, Orsay, France, 2002).
21. A. Blanc, T. Fusco, M. Hartung, L. M. Mugnier, and G.

Rousset, "Calibration of NAOS and CONICA static aberrations. Application of the phase diversity technique," Astron. Astrophys. **399**, 373–383 (2003).
22. P. J. Green, "Bayesian reconstructions from emission tomography data using a modified EM algorithm," IEEE Trans. Med. Imaging **9**, 84–93 (1990).
23. C. Bouman and K. Sauer, "A generalized gaussian image model for edge-preserving MAP estimation," IEEE Trans. Image Process. **2**, 296–310 (1993).
24. J. Idier and L. Blanc-Féraud, "Déconvolution en imagerie," in *Approche bayésienne pour les problèmes inverses*, J. Idier, ed. (Hermès, Paris, 2001), Chap. 6, pp. 139–165.
25. W. J. J. Rey, *Introduction to Robust and Quasi-Robust Statistical Methods* (Springer-Verlag, Berlin, 1983).
26. S. Brette and J. Idier, "Optimized single site update algorithms for image deblurring," in *Proceedings of the International Conference on Image Processing* (IEEE Computer Society, Press, Los Alamitos, Calif., 1996), pp. 65–68.
27. L. M. Mugnier, C. Robert, J.-M. Conan, V. Michau, and S. Salem, "Myopic deconvolution from wave-front sensing," J. Opt. Soc. Am. A **18**, 862–872 (2001).
28. L. Mugnier and G. Le Besnerais, "Problèmes inverses en imagerie optique à travers la turbulence," in *Approche bayésienne pour les problèmes inverses*, J. Idier, ed. (Hermès, Paris, 2001), Chap. 10, pp. 241–270.
29. H. R. Künsch, "Robust priors for smoothing and image restoration," Ann. Inst. Statist. Math. **46**, 1–19 (1994).
30. J. Högbom, "Aperture synthesis with a non-regular distribution of interferometer baselines," Astron. Astrophys. Suppl. Ser. **15**, 417–426 (1974).
31. P. Stetson, "DAOPHOT: a computer program for crowded-field stellar photometry," Publ. Astron. Soc. Pac. **99**, 191–222 (1987).
32. P. Magain, F. Courbin, and S. Sohy, "Deconvolution with correct sampling," Astrophys. J. **494**, 472–477 (1998).
33. K. F. Kaaresen, "Evaluation and applications of the iterated window maximization method for sparse deconvolution," IEEE Trans. Signal Process. **46**, 609–624 (1998).
34. F. Champagnat, Y. Goussard, S. Gautier, and J. Idier, "Déconvolution impulsionnelle," in *Approche bayésienne pour les problémes inverses*, J. Idier, ed. (Hermès, Paris, 2001), Chap. 5, pp. 115–138.
35. T. J. Holmes, "Blind deconvolution of speckle images quantum-limited incoherent imagery: maximum-likehood approach," J. Opt. Soc. Am. A **9**, 1052–1061 (1992).
36. E. Thiébaut and J.-M. Conan, "Strict *a priori* constraints for maximum-likelihood blind deconvolution," J. Opt. Soc. Am. A **12**, 485–492 (1995).
37. D. A. Fish, A. M. Brinicombe, E. R. Pike, and J. G. Walker, "Blind deconvolution by means of the Richardson–Lucy algorithm," J. Opt. Soc. Am. A **12**, 58–65 (1995).
38. S. M. Jefferies and J. C. Christou, "Restoration of astronomical images by iterative blind deconvolution," Astrophys. J. **415**, 862–874 (1993).
39. T. J. Schulz, "Multiframe blind deconvolution of astronomical images," J. Opt. Soc. Am. A **10**, 1064–1073 (1993).
40. Y.-L. You and M. Kaveh, "A regularization approach to joint blur identification and image restoration," IEEE Trans. Image Process. **5**, 416–428 (1996).
41. G. Rousset, "Wave-front sensors," *Adaptive Optics in Astronomy*, F. Roddier, ed. (Cambridge U. Press, Cambridge, UK, 1999), Chap. 5, pp. 91–130. See also Ref. 3.
42. S. Harder, "Reconstruction de la réponse impulsionnelle du système d'optique adaptative ADONIS à partir des mesures de son analyseur de surface d'onde et Étude photométrique de la variabilité des étoiles YY Orionis," Ph.D. thesis (Université Joseph Fourier, Grenoble 1, France, 1999).
43. Groupe Problèmes Inverses, "GPAV: une grande œuvre collective," internal report (Laboratoire des Signaux et Systèmes, CNRS/Supélec/Université Paris-Sud, Orsay, France, 1997).
44. D. P. Bertsekas, *Nonlinear Programming* (Athena Scientific, Belmont, Mass., 1995).
45. D. G. Luenberger, *Introduction to Linear and Nonlinear Programming* (Addison-Wesley, Reading, Mass., 1973).
46. D. M. Titterington, "General structure of regularization procedures in image reconstruction," Astron. Astrophys. **144**, 381–387 (1985).
47. Y. Biraud, "A new approach for increasing the resolving power by data processing," Astron. Astrophys. **1**, 124–127 (1969).
48. D. Commenges, "The deconvolution problem: fast algorithms including the preconditioned conjugate-gradient to compute a MAP estimator," IEEE Trans. Autom. Control **29**, 229–243 (1984).
49. O. Nakamura, S. Kawata, and S. Minami, "Optical microscope tomography. II. Nonnegative constraint by a gradient-projection method," J. Opt. Soc. Am. A **5**, 554–561 (1988).
50. G. Rousset, F. Lacombe, P. Puget, N. Hubin, E. Gendron, T. Fusco, R. Arsenault, J. Charton, P. Gigan, P. Kern, A.-M. Lagrange, P.-Y. Madec, D. Mouillet, D. Rabaud, P. Rabou, E. Stadler, and G. Zins, "NAOS, the first AO system of the VLT: on sky performance," in *Adaptive Optical System Technology II*, P. L. Wizinowich and D. Bonaccini, eds., Proc. SPIE **4839**, 140–149 (2002).
51. D. L. Snyder, M. I. Miller, L. J. Thomas, Jr., and D. G. Politte, "Noise and edge artifacts in maximum-likelihood reconstruction for emission tomography," IEEE Trans. Med. Imaging **6**, 228–237 (1987).
52. J.-M. Conan, T. Fusco, L. Mugnier, F. Marchis, C. Roddier, and F. Roddier, "Deconvolution of adaptive optics images: from theory to practice," in *Adaptive Optical Systems Technology*, P. Wizinowich, ed., Proc. SPIE **4007**, 913–924 (2000).
53. T. Fusco, "Correction partielle et anisoplanétisme en optique adaptative: traitement *a posteriori* et optique adaptative multiconjuguée," Ph.D. thesis (Université de Nice-Sophia Antipolis, Nice, France, 2000).
54. F. Marchis, I. de Pater, A. G. Davies, H. G. Roe, T. Fusco, D. Le Mignant, P. Descamps, B. A. Macintosh, and R. Prangé, "High-resolution Keck adaptive optics imaging of violent volcanic activity on Io," Icarus **160**, 124–131 (2002).
55. F. Marchis, "Imagerie à haute résolution angulaire des objets planétaires en optique adaptative. Application au volcanisme de Io," Ph.D. thesis (Université Paul Sabatier (Toulouse III), Toulouse, France, 2000).
56. A.-M. Lagrange, G. Chauvin, T. Fusco, E. Gendron, D. Rouan, M. Hartung, F. Lacombe, D. Mouillet, G. Rousset, P. Drossart, R. Lenzen, C. Moutou, W. Brandner, N. Hubin, Y. Clenet, A. Stolte, R. Schoedel, G. Zins, and J. Spyromilio, "First diffraction limited images at VLT with NAOS and CONICA," in *Instrumental Design and Performance for Optical/Infrared Ground-Based Telescopes*, M. Iye and A. F. M. Moorwood, eds., Proc. SPIE **4841**, 860–868 (2002).
57. R. Lenzen, M. Hartung, W. Brandner, G. Finger, N. N. Hubin, F. Lacombe, A.-M. Lagrange, M. D. Lehnert, A. F. M. Moorwood, and D. Mouillet, "NAOS-CONICA first on-sky results in a variety of observing modes," in *Instrumental Desigtn and Performance for Optical/Infrared Ground-Based Telescopes*, M. Iye and A. F. M. Moorwood, eds., Proc. SPIE **4841**, 944–952 (2002).
58. F. Marchis, R. Prangé, and T. Fusco, "A survey of Io's volcanism by adaptive optics observations in the 3.8 micron thermal band (1996–1999)," J. Geophys. Res. **106**, 33141–33160 (2001).
59. R. R. Howell, J. R. Spencer, J. D. Goguen, F. Marchis, R. Prangé, T. Fusco, B. D. L. , G. J. Veeder, J. A. Rathbun, G. S. Orton, A. J. Groeholski, and J. A. Stansberry, "Ground-based observations of volcanism on Io in 1999 and early 2000," J. Geophys. Res. **106**, 33–129 (2002).
60. F. Roddier, C. Roddier, J. E. Graves, M. J. Northcott, and T. Owen, "Neptune cloud structure and activity: ground based monitoring with adaptive optics," Icarus **136**, 168–172 (1998).
61. J.-M. Conan, T. Fusco, L. M. Mugnier, and F. Marchis, "MISTRAL: Myopic Deconvolution Method Applied to ADONIS and simulated VLT-NAOS Images," ESO Messenger **99**, 38–45 (2000).
62. G. Chauvin, F. Ménard, T. Fusco, A.-M. Lagrange, J.-L. Beuzit, D. Mouillet, and J.-C. Augereau, "Adaptive optics

imaging of MBM 12 association. Seven binaries and edge-on disk in a quadruple system," Astron. Astrophys. **394**, 949–956 (2002).
63. R. Jayawardhana and A. Brandeker, "Discovery of close companions to the nearby young stars HD 199143 and HD 358623," Astrophys. J. Lett. **561**, L111–L113 (2001).
64. G. Chauvin, T. Fusco, A.-M. Lagrange, D. Mouillet, J.-L. Beuzit, M. Thomson, J.-C. Augereau, F. Marchis, C. Dumas, and P. Lowrance, "No disk needed around HD 199143 B," Astron. Astrophys. **394**, 219–223 (2002).
65. A. Coustenis, E. Gendron, O. Lai, J.-P. Véran, J. Woillez, M. Combes, L. Vapillon, T. Fusco, L. Mugnier, and P. Rannou, "Images of Titan at 1.3 and 1.6 micron with adaptive optics at the CFHT," Icarus **154**, 501–515 (2001).
66. S. Gibbard, B. A. Macintosh, C. E. Max, I. de Pater, F. Marchis, H. Roe, D. S. Acton, O. Lai, P. Wizinowitch, P. Stomski, E. F. Young, and C. P. McKay, "Near-infrared observations of Titan from the W. M. Keck Telescope adaptive optics system," manuscript available from the authors, e.g., fmarchis@astron.berkeley.edu.
67. G. Chauvin, M. Thomson, C. Dumas, J.-L. Beuzit, P. Lowrance, T. Fusco, A.-M. Lagrange, B. Zuckerman, and D. Mouillet, "Adaptive optics imaging survey of the Tucana–Horologium association," Astron. Astrophys. **404**, 157–162 (2003).
68. D. Hestroffer, F. Marchis, T. Fusco, and J. Berthier, "Adaptive optics observations of asteroid (216) Kleopatra," Research Note, Astron. Astrophys. **394**, 339–343 (2002).
69. T. Fusco, J.-M. Conan, L. Mugnier, V. Michau, and G. Rousset, "Characterization of adaptive optics point spread function for anisoplanatic imaging. Application to stellar field deconvolution," Astron. Astrophys. Suppl. Ser. **142**, 149–156 (2000).